catalysts

MDPI

Article

AuPd/3DOM TiO_2 Catalysts: Good Activity and Stability for the Oxidation of Trichloroethylene

Xing Zhang, Yuxi Liu, Jiguang Deng, Kunfeng Zhang, Jun Yang, Zhuo Han and Hongxing Dai *

Beijing Key Laboratory for Green Catalysis and Separation, Key Laboratory of Beijing on Regional Air Pollution Control, Key Laboratory of Advanced Functional Materials, Education Ministry of China, Laboratory of Catalysis Chemistry and Nanoscience, Department of Chemistry and Chemical Engineering, College of Environmental and Energy Engineering, Beijing University of Technology, Beijing 100124, China; xingz@emails.bjut.edu.cn (X.Z.); yxliu@bjut.edu.cn (Y.L.); jgdeng@bjut.edu.cn (J.D.); kfzhang@emails.bjut.edu.cn (K.Z.); yangjun123@emails.bjut.edu.cn (J.Y.); hz102938@emails.bjut.edu.cn (Z.H.)
* Correspondence: hxdai@bjut.edu.cn; Tel.: +8610-6739-6118; Fax: +8610-6739-1983

Received: 19 November 2018; Accepted: 13 December 2018; Published: 18 December 2018

Abstract: Three-dimensionally ordered macroporous (3DOM) TiO_2-supported AuPd alloy (xAu$_y$Pd/3DOM TiO_2 (x = 0.87–0.91 wt%; y = 0.51–1.86)) catalysts for trichloroethylene (TCE) oxidation were prepared using the polymethyl methacrylate-templating and polyvinyl alcohol-protected reduction methods. The as-prepared materials possessed a good-quality 3DOM structure and a surface area of 49–53 m^2/g. The noble metal nanoparticles (NPs) with a size of 3–4 nm were uniformly dispersed on the surface of 3DOM TiO_2. The 0.91Au$_{0.51}$Pd/3DOM TiO_2 sample showed the highest catalytic activity with the temperature at a TCE conversion of 90% being 400 °C at a space velocity of 20,000 mL/(g h). Furthermore, the 0.91Au$_{0.51}$Pd/3DOM TiO_2 sample possessed better catalytic stability and moisture-resistant ability than the supported Au or Pd sample. The partial deactivation induced by H_2O introduction of 0.91Au$_{0.51}$Pd/3DOM TiO_2 was reversible, while that induced by CO_2 addition was irreversible. No significant influence on TCE conversion was observed after introduction of 100 ppm HCl to the reaction system over 0.91Au$_{0.51}$Pd/3DOM TiO_2. The lowest apparent activation energy (51.7 kJ/mol) was obtained over the 0.91Au$_{0.51}$Pd/3DOM TiO_2 sample. The doping of Au to Pd changed the TCE oxidation pathway, thus reducing formation of perchloroethylene. It is concluded that the high adsorbed oxygen species concentration, good low-temperature reducibility, and strong interaction between AuPd NPs and 3DOM TiO_2 as well as more amount of strong acid sites were responsible for the good catalytic activity, stability, and water- and HCl-resistant ability of 0.91Au$_{0.51}$Pd/3DOM TiO_2. We believe that 0.91Au$_{0.51}$Pd/3DOM TiO_2 may be a promising catalyst for the oxidative elimination of chlorine-containing volatile organics.

Keywords: 3D ordered macroporous titanium dioxide; AuPd alloy nanoparticle; supported AuPd catalyst; chlorine-containing volatile organic compounds; trichloroethylene oxidation

1. Introduction

Chlorine-containing volatile organic compounds (CVOCs) are widely used in industries as solvents, dry-cleaning agents, degreasing agents, synthetic resins, and pharmaceuticals, which are nowadays produced in considerable amounts. These CVOCs are harmful to the environment and human health [1,2]. Therefore, it is highly desired to find effective methods to remove the CVOCs. So far, there have been a number of technologies for CVOCs elimination. Because of its high efficiency and low operating temperatures, catalytic oxidation is considered as one of the most promising catalytic technologies [3]. Various catalysts, such as noble metals, transition-metal oxides, and perovskite-type oxides, have been developed for the oxidation of CVOCs [4,5]. Ideal catalytic combustion of CVOCs

is formation of water, carbon dioxide, and hydrogen chloride. Over transition-metal oxides, there was generation of volatile metal oxychlorides and intermediate by-products which promoted the loss of the active phases and refractory organics [4]. In contrast, supported noble metals showed good activity and resistance against volatilization [6], hence becoming the most prospect catalysts for elimination of the CVOCs. Since Hutchings et al. first report on the hydrochlorination of acetylene, the supported Au catalysts have obtained continuing attention [7]. For example, Liu et al. observed that the three-dimensionally ordered macroporous (3DOM) $La_{0.6}Sr_{0.4}MnO_3$-supported gold and meso-Co_3O_4-supported gold catalysts showed the $T_{90\%}$ of 170 and 138 °C for toluene oxidation at a space velocity (SV) of 20,000 mL/(g h) [8,9], respectively. In recent years, Pt or Pd alloyed with Au has been reported to exhibit excellent catalytic activity for H_2O_2 synthesis, N_2O decomposition, toluene oxidation, and methane combustion [10]. For example, Hutchings and coworkers found that Au could play an electron donor for Pd, the active catalyst owned a Pd-enriched surface, and the surface-bound oxygen-centered radicals played an important role in toluene activation over the Au–Pd/TiO_2 catalysts [11]. Working on the Au–Pd alloy catalysts for vinyl acetate synthesis, Chen et al. pointed out that the main role of Au in the bimetallic system was to isolate the Pd atoms, promoted the anticipant coupling of critical surface species, and reduced formation of the unexpected by-products [12].

In the past several years, titanium dioxide and its containing materials have gained much attention. Titanium dioxide is an environmentally friendly compound, which is often used as a component of photocatalytic or NH_3-SCR catalysts. Such a material possesses unique redox behaviors and strong acid-resistant ability [13]. The 3DOM structure with a large pore size (>50 nm) could immensely enhance mass transfer of the reactants and efficiently utilize active sites on the accessible surface of porous inner walls, hence improving the catalytic activity and selectivity for trichloroethylene (TCE) combustion [14]. However, studies on the use of 3DOM TiO_2 as support to generate the Au–Pd alloy/3DOM TiO_2 catalysts for CVOCs oxidation have not been seen in the literature.

Previously, we investigated the controlled preparation, characterization, and catalytic performance of numerous 3DOM-structued catalysts (e.g., Au–Pd/3DOM Co_3O_4 [15], Au–Pd/MnO_2 [16], and Au–Pd/3DOM $La_{0.6}Sr_{0.4}MnO_3$ [17]), and observed that most of them performed well in the oxidation of VOCs. Herein, we report the preparation of xAu$_y$Pd/3DOM TiO_2 (x = 0.87–0.91 wt%; y = 0.51–1.86) using the polymethyl methacrylate (PMMA)-templating and gas bubble-assisted polyvinyl alcohol (PVA)-protected reduction strategies. Based on the characterization and activity results, we found that adsorbed oxygen species concentration, low-temperature reducibility, and interaction between AuPd NPs and 3DOM TiO_2 influenced activity, stability, and water- and HCl-resistant ability of the catalysts.

2. Results and Discussion

2.1. Crystal Phase, Morphology, Pore Structure, and Surface Area

Figure 1 shows the phase structures of the 3DOM TiO_2, 0.89$Au_{1.86}$Pd/3DOM TiO_2, 0.87$Au_{0.95}$Pd/3DOM TiO_2, 0.91$Au_{0.51}$Pd/3DOM TiO_2, 0.93Au/3DOM TiO_2, and 0.89Pd/3DOM TiO_2 samples. All of the samples exhibited similar XRD patterns. The diffraction signals at 2θ = 25.3°, 36.5°, 37.8°, 38.6°, 48.0°, 53.9°, 55.1°, 62.7°, and 75.0° can be indexed to the (101), (103), (004), (112), (200), (105), (211), (204), and (215) crystal planes of the anatase-phase TiO_2 (JCPDS PDF# 21-1272) [18], respectively. No characteristic diffraction peaks assignable to the noble metal phases appeared, indicating formation of the highly dispersed noble metal NPs. It should be noted that the absence of XRD signals due to the noble metal phases might be also associated with their low loadings. According to the Scherrer equation using the FWHM of the (101) line of TiO_2, one can obtain the crystallite sizes (D) of TiO_2 that were in the range of 19.5–20.4 nm.

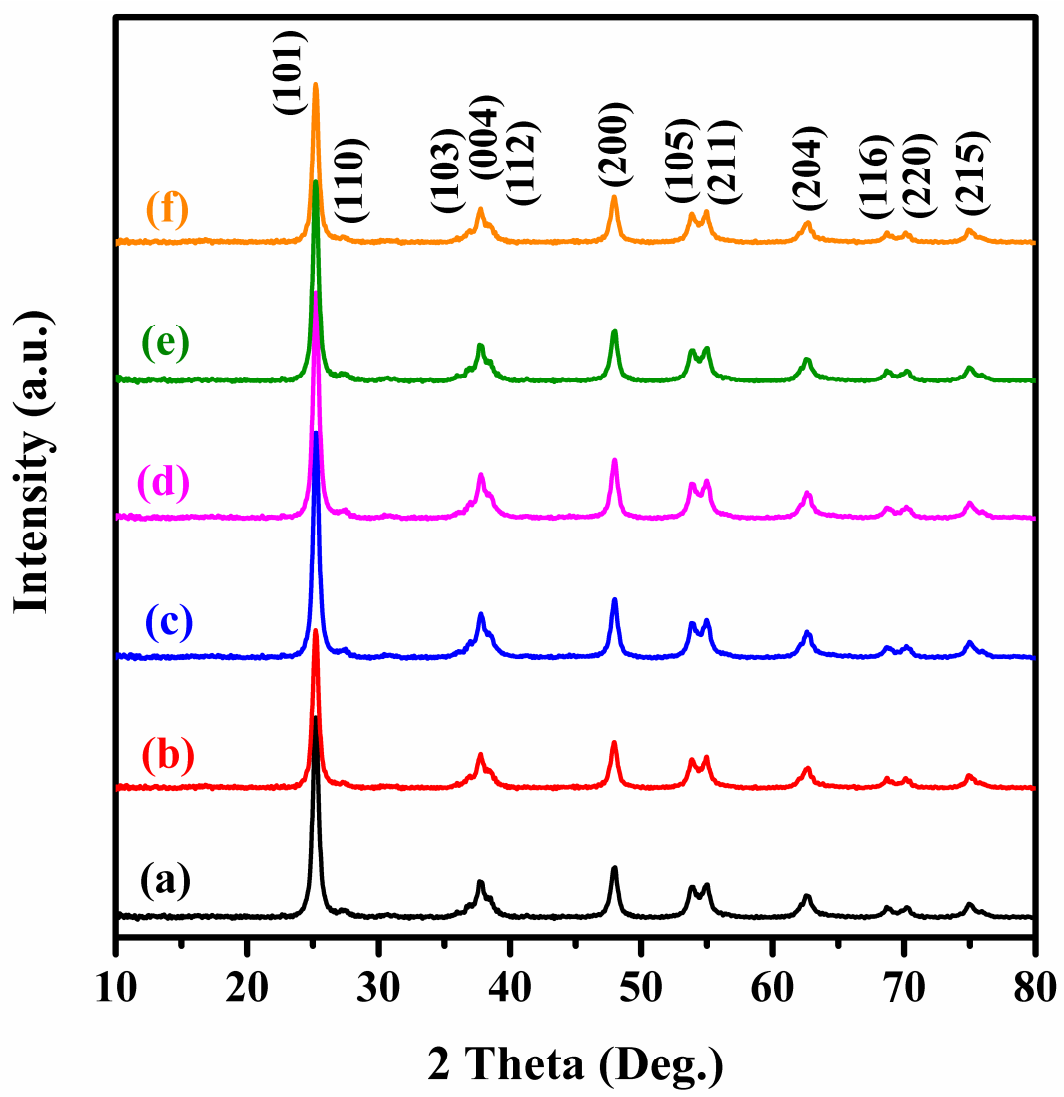

Figure 1. XRD patterns of (**a**) three-dimensionally ordered macroporous (3DOM) TiO_2, (**b**) $0.89Au_{1.86}Pd$/3DOM TiO_2, (**c**) $0.87Au_{0.95}Pd$/3DOM TiO_2, (**d**) $0.91Au_{0.51}Pd$/3DOM TiO_2, (**e**) 0.93Au/3DOM TiO_2, and (**f**) 0.89Pd/3DOM TiO_2.

Figures 2–4 exhibit the SEM, TEM, and HAADF–STEM images of the typical samples, respectively. It can be clearly seen that the 3DOM TiO_2, $0.89Au_{1.86}Pd$/3DOM TiO_2, $0.87Au_{0.95}Pd$/3DOM TiO_2, $0.91Au_{0.51}Pd$/3DOM TiO_2, 0.93Au/3DOM TiO_2, and 0.89Pd/3DOM TiO_2 samples possessed a high-quality 3DOM architecture with a pore size of 175–205 nm (Figure 2a–h). The sizes of 200 particles from TEM images (Figure 3a–l) were measured. It is found that the mean sizes (2.9–3.4 nm) of AuPd alloy NPs in xAu_yPd/3DOM TiO_2 were smaller than or similar to the mean sizes (3.2–3.5 nm) of Au and Pd NPs in 0.93Au/3DOM TiO_2 and 0.89Pd/3DOM TiO_2 (Table 1 and Figure S2). The interplanar crystal spacing of Au NPs in 0.93Au/3DOM TiO_2 was 0.234 nm (Figure 3j), which were identified to the (111) crystal face of Au NPs. The interplanar crystal spacing of Pd NPs in 0.89Pd/3DOM TiO_2 was 0.226 nm (Figure 3l), which was due to the fcc (111) crystal plane of Pd NPs. The lattice fringes (0.23 nm) were clearly observed in the AuPd NPs on the surface of 3DOM TiO_2, which were assigned to the fcc (111) crystal face of Au–Pd NPs. Furthermore, the intraplanar crystal spacing of 0.25 nm corresponded to the (101) crystal plane of 3DOM TiO_2. To further study the structures and compositions of the 3DOM TiO_2-supported AuPd NPs, we recorded the HAADF–STEM and EDS elemental mapping images (Figure 4) of the xAu_yPd/3DOM TiO_2 samples. Apparently, the Au, Pd, and/or AuPd NPs were well dispersed on the skeleton surface of the 3DOM TiO_2. The signal intensity

of the Au element (sapphirine in color) was similar to the signal intensity of the Pd element (pink in color), suggesting that the Au and Pd were uniformly mixed in the AuPd NPs. Such a uniform structure indicates that an AuPd alloy was formed within the AuPd NPs [15,16]. During the reduction processes, the mixed noble metal precursors were synchronously reduced to form the bimetallic AuPd alloy NPs because of its similar standard reduction potentials. The synergic effect of AuPd alloy and TiO_2 could provide ample low-coordination unsaturated metal sites or oxygen vacancies, which were active sites for adsorption and activation of molecular oxygen.

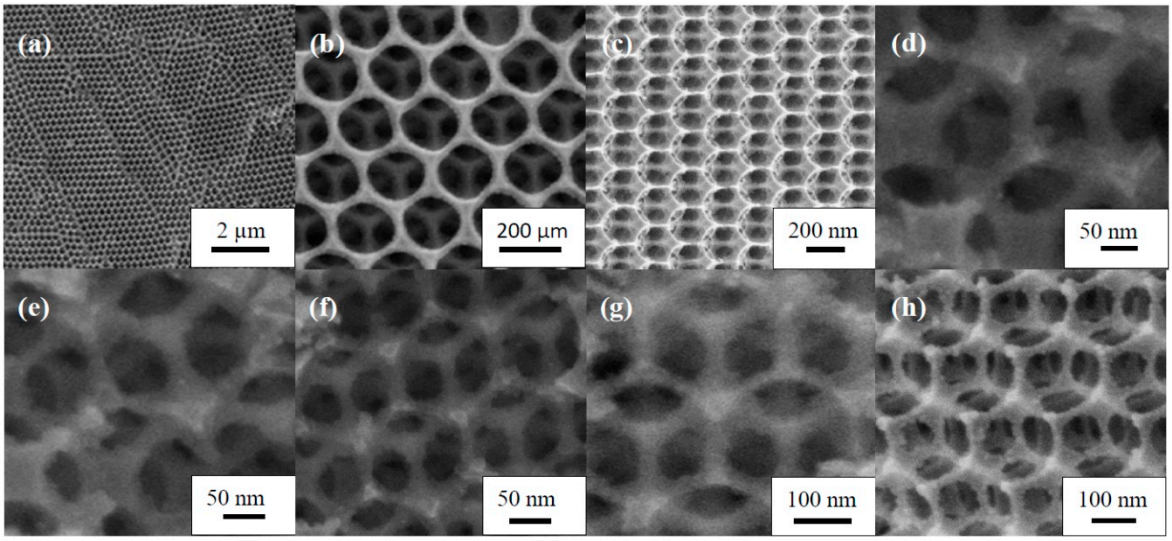

Figure 2. SEM images of (**a**,**b**) 3DOM TiO_2, (**c**,**d**) $0.89Au_{1.86}Pd$/3DOM TiO_2, (**e**) $0.87Au_{0.95}Pd$/3DOM TiO_2, (**f**) $0.91Au_{0.51}Pd$/3DOM TiO_2, (**g**) 0.93Au/3DOM TiO_2, and (**h**) 0.89Pd/3DOM TiO_2.

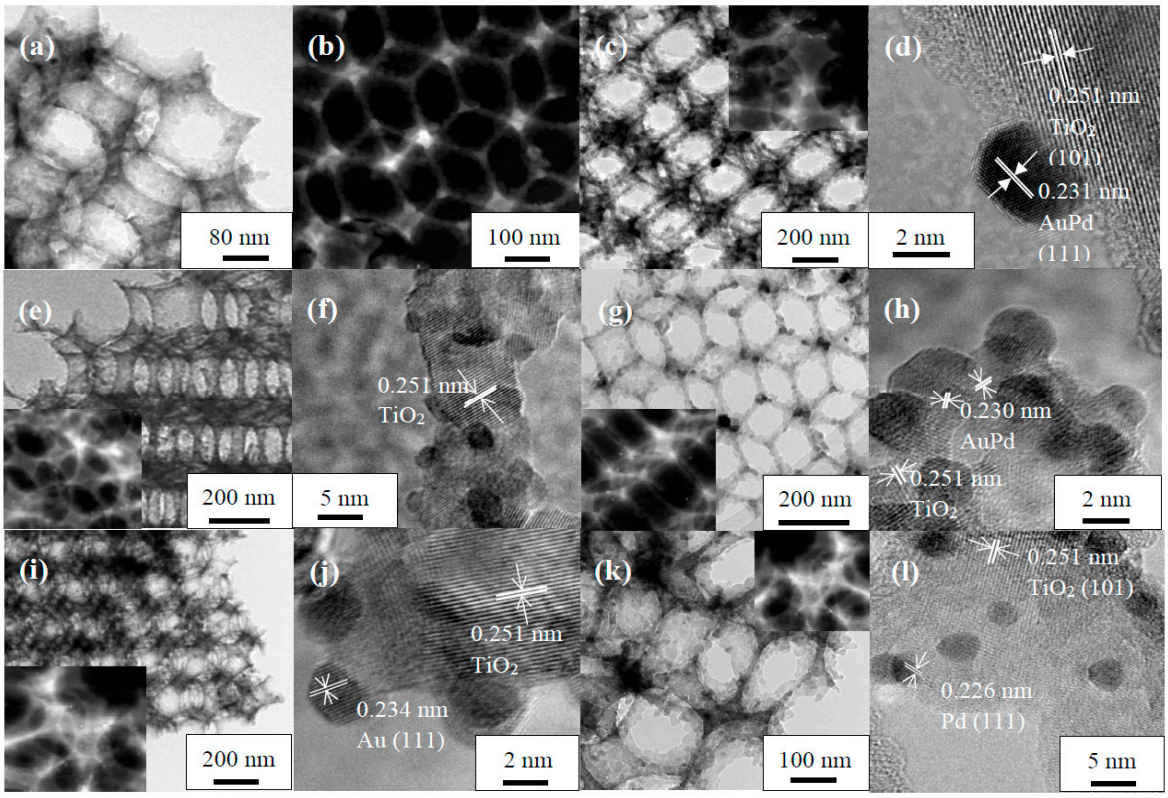

Figure 3. TEM images of (**a**,**b**) 3DOM TiO_2, (**c**,**d**) $0.89Au_{1.86}Pd$/3DOM TiO_2, (**e**,**f**) $0.87Au_{0.95}Pd$/3DOM TiO_2, (**g**,**h**) $0.91Au_{0.51}Pd$/3DOM TiO_2, (**i**,**j**) 0.93Au/3DOM TiO_2, and (**k**,**l**) 0.89Pd/3DOM TiO_2.

Table 1. Actual noble metal contents, TiO_2 crystallite sizes (*D*), noble metal particle sizes, macro- and mesopore diameters, BET surface areas, and pore volumes of the as-prepared samples.

Sample	Actual Au Content [a] (wt%)	Actual Pd Content [a] (wt%)	Actual Au/Pd Molar Ratio [a] (mol/mol)	*D* [b] (nm)	Noble Metal Particle Size [c] (nm)	Mesopores Diameter [d] (nm)	Macropores Diameter [e] (nm)	BET Surface Area [e] (m^2/g)	Pore Volume [e] (cm^3/g)
3DOM TiO_2	–	–	–	20.1	-	180–200	3.1–4.2	53.3	0.209
$0.89Au_{1.86}Pd$/3DOM TiO_2	0.69	0.20	1.86	19.6	3.4	175–194	2.6–4.1	50.2	0.205
$0.87Au_{0.95}Pd$/3DOM TiO_2	0.56	0.31	0.95	20.4	3.2	186–205	2.9–4.4	49.5	0.208
$0.91Au_{0.51}Pd$/3DOM TiO_2	0.44	0.47	0.51	19.8	2.9	180–201	2.8–4.3	51.2	0.210
0.93Au/3DOM TiO_2	0.93	–	–	20.3	3.2	176–195	2.7–4.2	52.1	0.196
0.89Pd/3DOM TiO_2	–	0.89	–	19.5	3.5	178–194	3.0–4.3	50.6	0.190

[a] The data were determined by the ICP–AES technique; [b] The data were estimated based on the Scherrer equation using the full width at half maximum (FWHM) of the (101) lattice plane of TiO_2; [c] The data were measured according to high-resolution transmission electron microscopic (HRTEM) images of the noble metal nanoparticles (NPs) on the surface of the samples; [d] The data were estimated according to the SEM images; [e] The data were determined by the BET method.

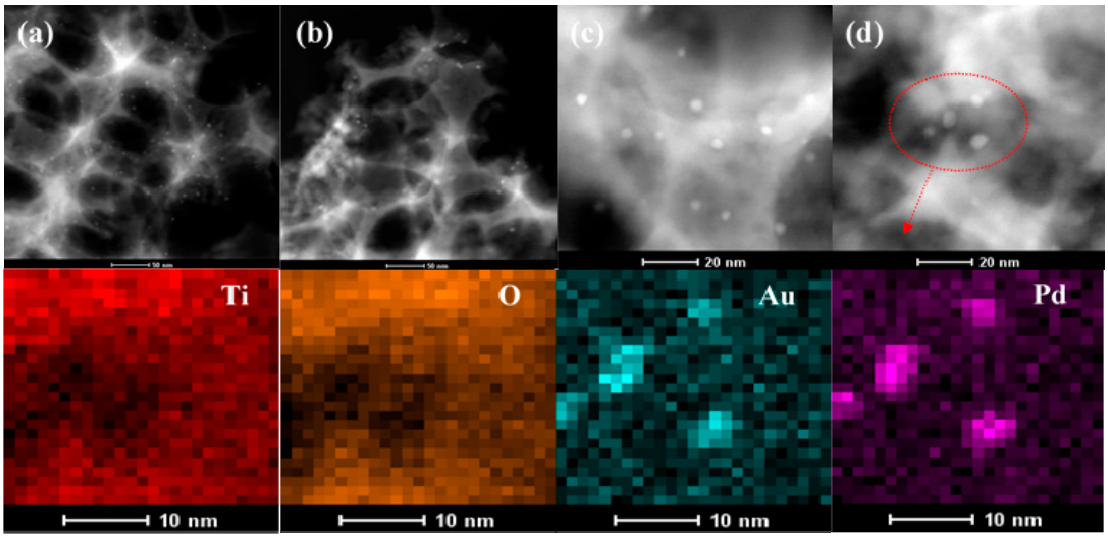

Figure 4. (**a**–**d**) High-angle annular dark field (HAADF) and elemental scanning images of the $0.91Au_{0.51}Pd/3DOM\ TiO_2$.

Figure S3 shows the N_2 adsorption–desorption isotherms and pore-size distributions of the 3DOM TiO_2, $0.89Au_{1.86}Pd/3DOM\ TiO_2$, $0.87Au_{0.95}Pd/3DOM\ TiO_2$, $0.91Au_{0.51}Pd/3DOM\ TiO_2$, $0.93Au/3DOM\ TiO_2$, and $0.89Pd/3DOM\ TiO_2$ samples. Each sample exhibited a type II isotherm with an H3 hysteresis loop in the relative pressure (p/p_0) range of 0.8–1.0 and a small H2-type hysteresis loop in the p/p_0 range of 0.2–0.8. The existence of H3 hysteresis loop indicates existence of the slit-shaped macropores in the materials [19]. The low-pressure portion of the almost linear middle section of each isotherm (which could be attributed to the multilayer adsorption) also suggests formation of macropores [20]. The appearance of H2 hysteresis loop indicates that mesoporous existed in the skeleton of 3DOM TiO_2. There were meso- or nanopores (2.6–4.4 nm) and macro- or submicropores (175–205 nm) in these samples (Table 1), which were proven by the SEM and TEM observations and pore-size distributions of the samples. The samples possessed hierarchical pore structures (textural meso- or nanopores and open macro- or submicropores). Surface areas (49.5–52.1 m^2/g) of the $xAu_yPd/3DOM\ TiO_2$, $0.93Au/3DOM\ TiO_2$, and $0.89Pd/3DOM\ TiO_2$ samples were slightly lower than that (53.3 m^2/g) of the 3DOM TiO_2 support. All of the samples possessed a pore volume of 0.190–0.210 cm^3/g.

2.2. Metal Oxidation State and Surface Element Composition

We use the XPS technique to measure the surface element compositions and surface species of the samples. O 1s, Ti 2p, Pd 3d, and Au 4f XPS spectra of the 3DOM TiO_2, $0.89Au_{1.86}Pd/3DOM\ TiO_2$, $0.87Au_{0.95}Pd/3DOM\ TiO_2$, $0.91Au_{0.51}Pd/3DOM\ TiO_2$, $0.93Au/3DOM\ TiO_2$, and $0.89Pd/3DOM\ TiO_2$ samples were recorded, as shown in Figure 5. Using the CasaXPS (computer aided surface analysis for X-ray photoelectron spectroscopy) software to perform the curve-fitting of the spectra, one can obtain the XPS data (Table S1). The asymmetric O 1s XPS signal could be decomposed to three components at binding energy (BE) = 529.6, 531.7, and 533.3 eV (Figure 5A), ascribable to the surface lattice oxygen (O_{latt}), adsorbed oxygen (O_{ads}, e.g., O_2^-, O_2^{2-} or O^-), and carbonate or adsorbed water species [15,16], respectively. According to the quantitative analysis on the three peaks, the $0.91Au_{0.51}Pd/3DOM\ TiO_2$ sample showed the highest O_{ads}/O_{latt} molar ratio (Table 2). Since the O_{ads} species was important for the deep oxidation of organics, the $0.91Au_{0.51}Pd/3DOM\ TiO_2$ sample would be expected to show good catalytic activity for TCE combustion. As shown in Figure 5B, the BEs of Ti $2p_{1/2}$ and Ti $2p_{3/2}$ of TiO_2 were 464.1 and 458.3 eV, respectively, which were assigned to the surface Ti^{4+} species. Each of the Au 4f spectra of the Au-containing samples could be decomposed into six components (Figure 5C): the two components at BE = 83.4 and 87.3 eV were assigned to the surface Au^0 species, while the other

four components at BE = 84.3, 85.8, 88.4, and 89.9 eV were attributed to the surface $Au^{\delta+}$ species [21]. There were higher $Au^{\delta+}/Au^0$ molar ratios (0.29–0.36) on the supported Au–Pd alloy samples than that (0.21) on the supported Au sample. It is well known that a higher $Au^{\delta+}/Au^0$ molar ratio stands for a stronger ability in activating oxygen molecules, thus favoring the oxidation of VOCs. Each of the Pd 3d XPS spectra of the Pd-containing samples was deconvoluted into four components (Figure 5D): the two components at BE = 335.5 and 340.7 eV were ascribed to the surface Pd^0 species, whereas the other two components at BE = 337.8 and 342.7 eV were attributed to the surface Pd^{2+} species [22]. There were higher Pd^{2+}/Pd^0 molar ratios (0.65–0.77) on the surface of xAu$_y$Pd/3DOM TiO_2 than that (0.63) on the surface of 0.89Pd/3DOM TiO_2, indicating that Au inclusion could increase the surface Pd^{2+} concentration of the sample. Such a conclusion was well consistent with Hutchings' finding that Au could act as an electron promoter for Pd in bimetallic AuPd NPs on TiO_2 [23]. The active $Au^{\delta+}$ and Pd^{2+} species located at the interface between AuPd NPs and TiO_2 were beneficial for improving O_2 adsorption and activation, leading to an increase in density of active oxygen species.

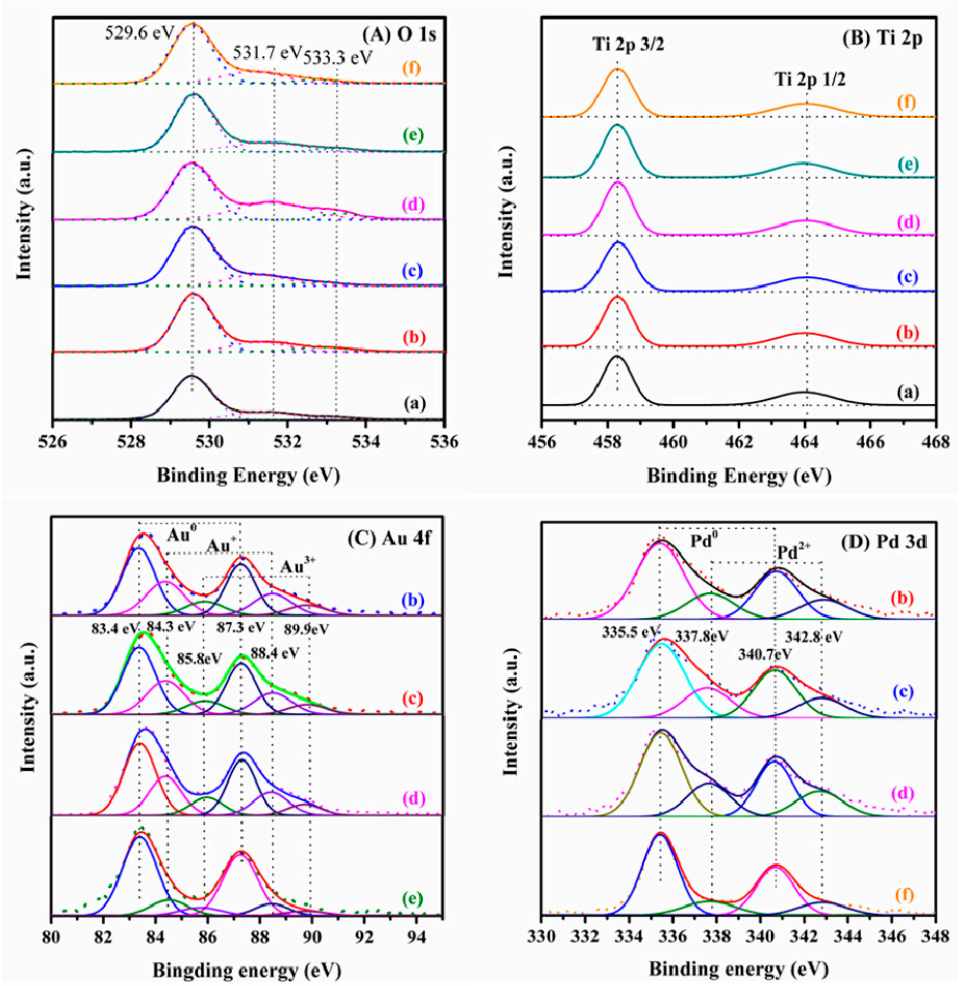

Figure 5. (**A**) O 1s, (**B**) Ti 2p, (**C**) Au 4f, and (**D**) Pd 3d XPS spectra of (**a**) 3DOM TiO_2, (**b**) 0.89Au$_{1.86}$Pd/3DOM TiO_2, (**c**) 0.87Au$_{0.95}$Pd/3DOM TiO_2, (**d**) 0.91Au$_{0.51}$Pd/3DOM TiO_2, (**e**) 0.93Au/3DOM TiO_2, and (**f**) 0.89Pd/3DOM TiO_2.

2.3. Low-Temperature Reducibility and Oxygen Species

It is well known that catalytic activity largely depends on the redox property of a sample. In this work, the H_2-TPR technique was used to investigate the reducibility of the 3DOM TiO_2, 0.89Au$_{1.86}$Pd/3DOM TiO_2, 0.87Au$_{0.95}$Pd/3DOM TiO_2, 0.91Au$_{0.51}$Pd/3DOM TiO_2, 0.93Au/3DOM TiO_2, and 0.89Pd/3DOM TiO_2 samples, and their profiles are shown in Figure 6A. For the 3DOM

TiO_2 sample, there were two reduction peaks at 303 and 508 °C, which were assigned to the removal of adsorbed oxygen species on the surface of TiO_2 and the reduction of Ti^{4+} to Ti^{2+} [24]. When Au, Pd or Au–Pd NPs were loaded on the skeleton surface of 3DOM TiO_2, the reduction peaks were shifted to lower temperatures (28–265 and 415–441 °C, respectively), indicating that the noble metal NPs promoted the reduction of 3DOM TiO_2 through the strong interaction between noble metal NPs and 3DOM TiO_2. The higher intensity of the low-temperature peak was due to the reduction of oxidized noble metals as well as the removal of adsorbed oxygen species on the surface of TiO_2. The improvement in low-temperature reducibility would favor the increase in catalytic performance. Among these samples, $0.91Au_{0.51}Pd$/3DOM TiO_2 showed the lowest reduction temperature (218 °C), suggesting that this sample possessed the best low-temperature reducibility. The hydrogen consumption can be obtained by quantitative analysis of the reduction peaks in the H_2-TPR profiles of the samples. The H_2 consumption (14.2 mmol/g) of 3DOM TiO_2 was lower than that (15.3–17.2 mmol/g) of xAu_yPd/3DOM TiO_2 (Table 2). It is better to use the initial H_2 consumption rate to evaluate the low-temperature reducibility of a catalyst [25], and the results are shown in Figure 6B. It is observed that the initial H_2 consumption rate (i.e., low-temperature reducibility) decreased in the order of $0.91Au_{0.51}Pd$/3DOM TiO_2 > 0.89Pd/3DOM TiO_2 > $0.87Au_{0.95}Pd$/3DOM TiO_2 > $0.89Au_{1.86}Pd$/3DOM TiO_2 > 0.93Au/3DOM TiO_2 > 3DOM TiO_2, in good agreement with the sequence in catalytic activity of the samples (shown below). It is therefore concluded that catalytic activity was closely related to low-temperature reducibility of the sample.

Table 2. Quantitative results of XPS, oxygen temperature-programmed desorption (O_2-TPD), and hydrogen temperature-programmed reduction (H_2-TPR) characterization of the samples.

Sample	Surface Element Composition [a]			O_2 Desorption [b] (mmol/g)			H_2 Consumption [c] (mmol/g)		
	$Au^{\delta+}/Au^0$ Molar Ratio	Pd^{2+}/Pd^0 Molar Ratio	O_{ads}/O_{latt} Molar Ratio	50–450 °C	450–800 °C	Total	<350 °C	≥350 °C	Total
3DOM TiO_2	–	–	0.31	0.46	1.92	2.38	2.8	11.4	14.2
$0.89Au_{1.86}Pd$/3DOM TiO_2	0.29	0.65	0.45	0.98	2.21	3.19	10.2	5.4	15.6
$0.87Au_{0.95}Pd$/3DOM TiO_2	0.31	0.68	0.47	1.03	2.18	3.21	10.8	5.3	16.1
$0.91Au_{0.51}Pd$/3DOM TiO_2	0.36	0.77	0.56	1.16	2.31	3.47	12.9	4.3	17.2
0.93Au/3DOM TiO_2	0.21	–	0.43	0.92	2.13	3.05	9.7	5.7	15.4
0.89Pd/3DOM TiO_2	–	0.63	0.49	1.08	2.20	3.28	11.2	5.1	16.3

[a] The data were estimated by making quantitative analysis on the XPS spectra of the samples; [b] The data were calculated by making quantitative analysis on the O_2-TPD profiles of the samples; [c] The data were obtained by making quantitative analysis on the H_2-TPR profiles of the samples.

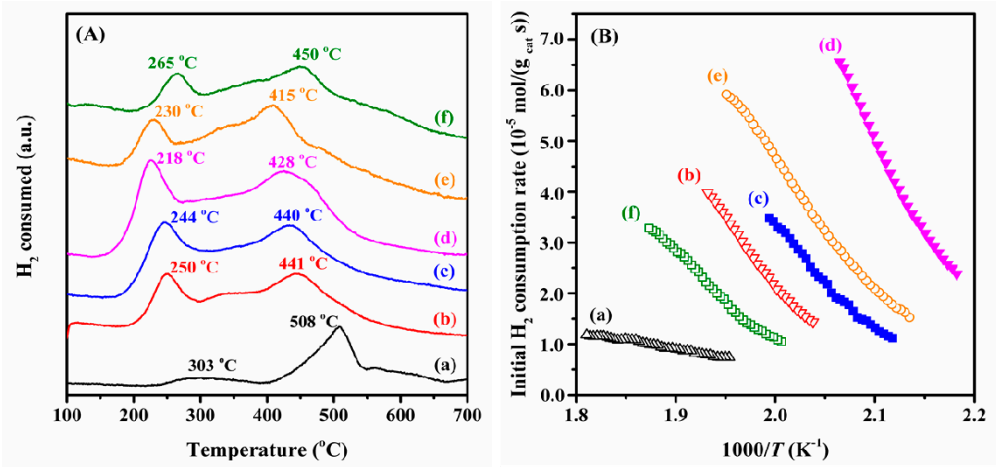

Figure 6. (**A**) H_2-TPR profiles and (**B**) initial H_2 consumption rate versus inverse temperature of (**a**) 3DOM TiO_2, (**b**) $0.89Au_{1.86}Pd$/3DOM TiO_2, (**c**) $0.87Au_{0.95}Pd$/3DOM TiO_2, (**d**) $0.91Au_{0.51}Pd$/3DOM TiO_2, (**e**) 0.89Pd/3DOM TiO_2, and (**f**) 0.93Au/3DOM TiO_2.

The ability to activate oxygen is closely related to the catalytic performance for VOCs oxidation. Figure 7 shows the O_2-TPD profiles of the 3DOM TiO_2, $0.89Au_{1.86}Pd$/3DOM TiO_2, $0.87Au_{0.95}Pd$/3DOM TiO_2, $0.91Au_{0.51}Pd$/3DOM TiO_2, 0.93Au/3DOM TiO_2, and 0.89Pd/3DOM TiO_2 samples. Each profile displayed two oxygen desorption peaks at ca. 170 and 680 °C, which corresponded to the low-temperature and high-temperature desorption of oxygen. It is known that the adsorbed oxygen generally transforms in the order of O_2 (gas) → O_2 (ads) → O_2^- (ads) → O_2^{2-} (ads) → O^- (ads) → O^{2-} (lattice) [26]. From the results reported in the literature, we tentatively attributed the low-temperature peak to desorption of the chemisorbed oxygen (O_{ads}, e.g., O_2^-, O_2^{2-} or O^-) species, which could be easier desorbed from the catalyst surface. The high-temperature peak was associated with desorption of the lattice oxygen (O_{latt}) species [21]. The adsorption and desorption of oxygen could be enhanced by loading precious metal alloys on the surface of titanium dioxide. It is seen from Table 2 that the total O_2 desorption (3.05–3.47 mmol/g) of xAu_yPd/3DOM TiO_2 was higher than the total O_2 desorption (2.28 mmol/g) of 3DOM TiO_2. At the same time, the desorbed oxygen species below 450 °C decreased in the order of $0.91Au_{0.51}Pd$/3DOM TiO_2 (1.16 mmol/g) > 0.89Pd/3DOM TiO_2 (1.08 mmol/g) > $0.87Au_{0.95}Pd$/3DOM TiO_2 (1.03 mmol/g) > $0.89Au_{1.86}Pd$/3DOM TiO_2 (0.98 mmol/g) > 0.93Au/3DOM TiO_2 (0.92 mmol/g) > 3DOM TiO_2 (0.46 mmol/g). It was reported that the ability to activate O_2 is associated with the surface oxygen vacancy density [27]. Loading of Au_yPd alloy NPs might increase the surface oxygen-deficient density of 3DOM TiO_2 due to existence of the strong interaction between Au_yPd NPs and 3DOM TiO_2. The Au_yPd NPs possessed a strong electron-donating ability to activate molecular oxygen, therefore favoring the adsorption and activation of oxygen.

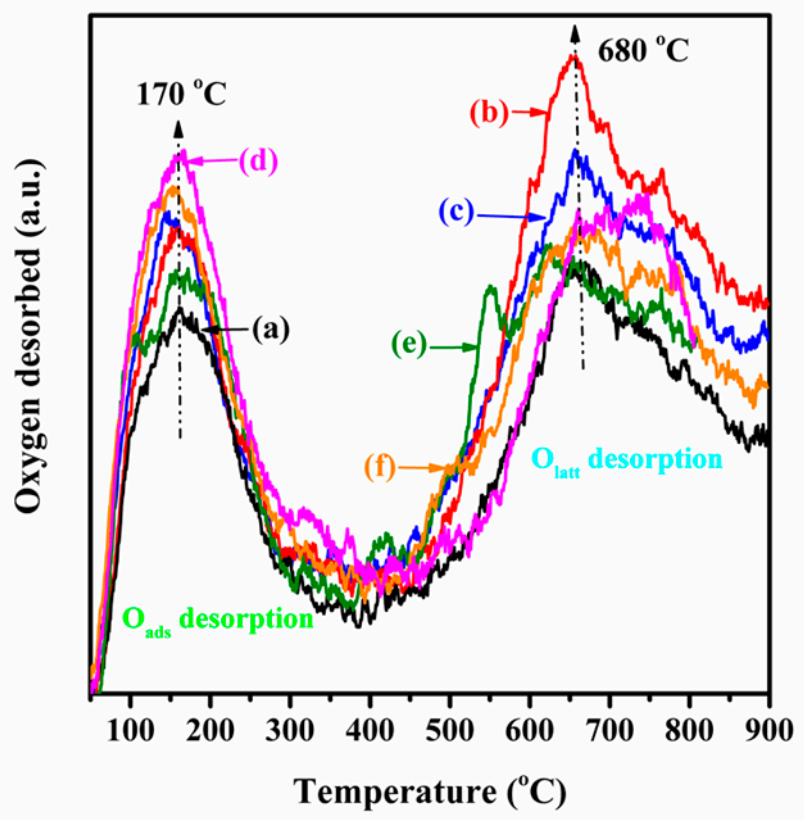

Figure 7. O_2-TPD profiles of (**a**) 3DOM TiO_2, (**b**) $0.89Au_{1.86}Pd$/3DOM TiO_2, (**c**) $0.87Au_{0.95}Pd$/3DOM TiO_2, (**d**) $0.91Au_{0.51}Pd$/3DOM TiO_2, (**e**) 0.93Au/3DOM TiO_2, and (**f**) 0.89Pd/3DOM TiO_2.

2.4. Surface Acid Property

Surface acid properties of the samples were characterized by the NH_3-TPD technique, and their profiles are shown in Figure 8. The desorption peak at 50–450 °C was assigned to the successive desorption of ammonia physically adsorbed at the weak acid sites, and the desorption of NH_3 at the weak acid sites were observed in all of the samples. The peaks at 450–900 °C corresponded to the strong acid sites. The NH_3 desorption (peaks at 450–900 °C) from the 3DOM TiO_2 sample was weaker than that from the $0.91Au_{0.51}Pd$/3DOM TiO_2 sample, indicating a rather low amount of NH_3 adsorption on the former sample [28]. The relative area (A_{strong}/A_{weak}) of the desorption peaks corresponds to the amount of ammonia that desorbs from the sample, and could be taken as a standard to quantify the acidity of the sample [29,30]. Obviously, the amount (A_{strong}/A_{weak} = 0.50) of strong acid sites in $0.91Au_{0.51}Pd$/3DOM TiO_2 was more than that (A_{strong}/A_{weak} = 0.12) in 3DOM TiO_2, suggesting that AuPd doping could enhance the acidity of the sample. According to the literature [31], strong acid sites were more important than weak acid sites for the deep oxidation of CVOCs. The weak acidic sites were related to the adsorption of TCE, while the strong acid sites were associated with the deep oxidation of TCE.

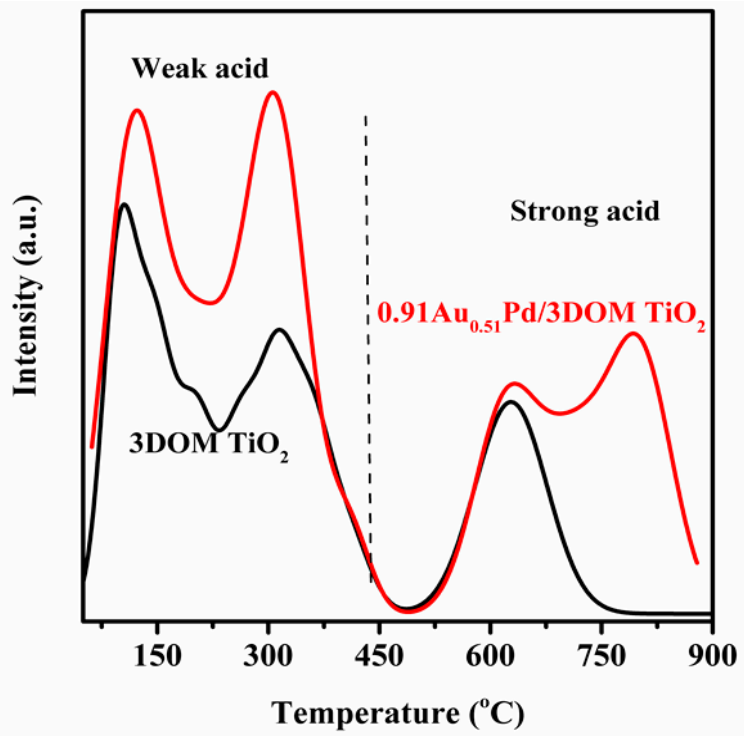

Figure 8. NH_3-TPD profiles of 3DOM TiO_2 and $0.91Au_{0.51}Pd$/3DOM TiO_2.

2.5. Catalytic Performance

Figure 9A shows catalytic activities of the 3DOM TiO_2, $0.89Au_{1.86}Pd$/3DOM TiO_2, $0.87Au_{0.95}Pd$/3DOM TiO_2, $0.91Au_{0.51}Pd$/3DOM TiO_2, 0.93Au/3DOM TiO_2, and 0.89Pd/3DOM TiO_2 samples for TCE combustion. It is convenient to compare catalytic activities of the samples using the reaction temperatures $T_{10\%}$, $T_{50\%}$, and $T_{90\%}$ (corresponding to TCE conversion = 10, 50, and 90%), as summarized in Table 3. TCE could not be completely oxidized over 3DOM TiO_2 (43% TCE conversion was obtained at 480 °C). After loading of Au, Pd, or Au_yPd, however, catalytic activity was obviously enhanced. For example, the $T_{10\%}$, $T_{50\%}$, and $T_{90\%}$ over $0.91Au_{0.51}Pd$/3DOM TiO_2 were 255, 354, and 400 °C at SV = 20,000 mL/(g h), respectively, much lower than those (294, 419, and 480 °C) over 0.93Au/3DOM TiO_2, those (283, 401, and 479 °C) over $0.89Au_{1.86}Pd$/3DOM TiO_2, those (270, 386, and 462 °C) over $0.87Au_{0.95}Pd$/3DOM TiO_2, and those (261, 371, and 435 °C) over

0.89Pd/3DOM TiO_2. Apparently, catalytic activity decreased in the sequence of $0.91Au_{0.51}Pd$/3DOM TiO_2 > 0.89Pd/3DOM TiO_2 > $0.87Au_{0.95}Pd$/3DOM TiO_2 > $0.89Au_{1.86}Pd$/3DOM TiO_2 > 0.93Au/3DOM TiO_2 > 3DOM TiO_2. Figure 9B shows the Arrhenius plots for TCE oxidation at TCE conversion <20% and SV = 20,000 mL/(g h) over the prepared catalysts. According to the slopes of the well linear Arrhenius plots, we calculate the apparent activation energies (E_a) of TCE oxidation over the prepared catalysts, as summarized in Table 3. Previous works have reported that the oxidation of CVOCs over Ru/Al_2O_3 [32], $LaMn_{1+x}O_3$ [33], Cr_2O_3 [34], and $Mn_xCe_{1-x}O_2$/HZSM–5 [35] fellow the reaction mechanism of first-order toward CVOC concentration and zero-order toward O_2 concentration. In the present, we can reasonably presume that TCE oxidation in the presence of excess oxygen (TCE/O_2 molar ratio = 1/1090) obeyed a first-order reaction mechanism with respect to TCE concentration (c): $r = -k\,c = (-A\,\exp(-E_a/RT))\,c$, in which r, k, A, and E_a are the reaction rate (mol/s), rate constant (s^{-1}), pre-exponential factor, and apparent activation energy (kJ/mol), respectively. It is well known that the lower the apparent activation energy (E_a), the easier the complete oxidation of an organic compound over the catalyst, and hence the better is the catalytic performance. The discrepancy in E_a of the samples could reflect their different catalytic activities. Obviously, the E_a increased in the sequence of $0.91Au_{0.51}Pd$/3DOM TiO_2 (51.7 kJ/mol) < 0.89Pd/3DOM TiO_2 (59.1 kJ/mol) < $0.87Au_{0.95}Pd$/3DOM TiO_2 (63.5 kJ/mol) < $0.89Au_{1.86}Pd$/3DOM TiO_2 (66.2 kJ/mol) < 0.93Au/3DOM TiO_2 (71.4 kJ/mol) < 3DOM TiO_2 (97.6 kJ/mol), with the $0.91Au_{0.51}Pd$/3DOM TiO_2 sample exhibiting the lowest E_a. Such a sequence agrees with the order in catalytic activity of these samples.

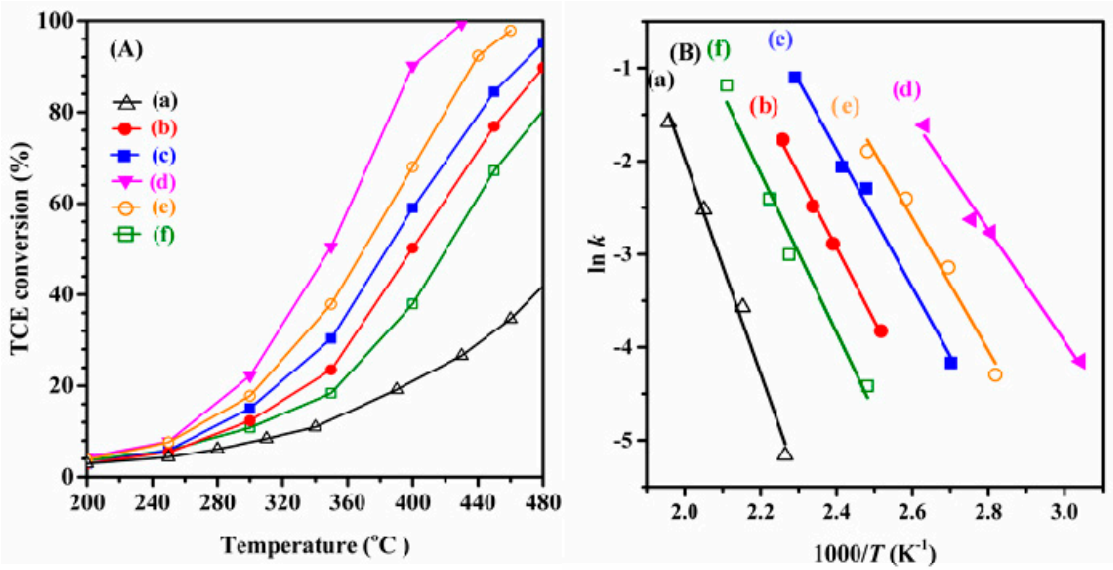

Figure 9. (**A**) Trichloroethylene (TCE) conversion as a function of temperature and (**B**) ln k versus inverse temperature over (**a**) 3DOM TiO_2, (**b**) $0.89Au_{1.86}Pd$/3DOM TiO_2, (**c**) $0.87Au_{0.95}Pd$/3DOM TiO_2, (**d**) $0.91Au_{0.51}Pd$/3DOM TiO_2, (**e**) 0.89Pd/3DOM TiO_2, and (**f**) 0.93Au/3DOM TiO_2.

Table 3. Catalytic activities, HCl selectivities (S_{HCl}), reaction rates, turnover frequencies (TOF), and apparent activation energies (E_a) at a SV of 20,000 mL/(g h) of the samples.

Catalyst	Catalytic Activity				TCE oxidation at 300 °C		E_a (kJ/mol)
	$T_{10\%}$ (°C)	$T_{50\%}$ (°C)	$T_{90\%}$ (°C)	S_{HCl} [a] (%)	Reaction Rate (μmol/($g_{Noble\ metal}$ s))	$TOF_{Noble\ metal}$ ($\times 10^{-3}$ s^{-1})	
3DOM TiO_2	320	–	–	32.3	–	–	97.6
$0.89Au_{1.86}Pd$/3DOM TiO_2	283	401	479	85.1	28.1	0.54	66.2
$0.87Au_{0.95}Pd$/3DOM TiO_2	270	386	462	88.4	36.5	0.71	63.5
$0.91Au_{0.51}Pd$/3DOM TiO_2	255	354	400	94.2	50.4	0.96	51.7
0.93Au/3DOM TiO_2	294	419	–	82.9	24.6	0.47	71.4
0.89Pd/3DOM TiO_2	261	371	435	91.6	45.1	0.85	59.1

[a] S_{HCl} = [HCl]/([HCl] + 2[Cl_2]) × 100%, which was measured at 435 °C.

To compare catalytic properties of the as-prepared samples, we calculate the TCE reaction rates (normalized by per gram of catalyst) and turnover frequencies (TOFs; TOFs = xC_0/n, x = the conversion at a certain temperature, C_0 (mol/s) = the initial TCE concentration per second, and n (mol) = the molar amount of metal or oxide (M = Au, Pd, Au_yPd, or TiO_2)), as listed in Table 3. Obviously, the $0.91Au_{0.51}Pd/3DOM\ TiO_2$ sample possessed the TCE reaction rate (50.4 μmol/($g_{Noble\ metal}$ s)) and the highest TOF (0.96×10^{-3} s^{-1}) at 300 °C. In the past years, there have been a number of works on the oxidation of TCE over various catalysts in the literature, and their typical activities are listed in Table S2. It can be observed that the TCE oxidation rate at 250 °C (2.69×10^{-7} mol/(g_{cat} s)) over $0.91Au_{0.51}Pd/3DOM\ TiO_2$ was much higher than those ((1.12–1.13) $\times 10^{-7}$ mol/(g_{cat} s)) over CeMn-HT-N6A4 [36] and 1.02 wt% Ru/TiO_2 (P25) [37], those ((2.67–9.76) $\times 10^{-8}$ mol/(g_{cat} s)) over $Ce_{0.15}Zr_{0.85}O_2$ [38], $LaMn_{1.2}O_3$ [33], 4Ce1Cr-$(NH_4)_2CO_3$ [39], and 3.5 wt% VO_x/TiO_2-SG [40], and those ((2.67–7.05) $\times 10^{-9}$ mol/(g_{cat} s)) over 4.3 wt% Mn/H-ZSM-5 [41], 0.42 wt% Pd/Al_2O_3 [42], and $CoFeAlO_x$ [43].

The analysis on the effluent gas mixture of TCE oxidation reveals that the reaction products were mainly composed of CO_x (CO_x = CO_2 + CO), H_2O, HCl, and Cl_2, and the other carbon-containing byproduct was only C_2Cl_4. Figure S4 shows the C_2Cl_4 concentration versus temperature over the as-obtained samples at SV = 20,000 mL/(g h). Over the 3DOM TiO_2 sample, a low concentration of C_2Cl_4 at T_{max} (temperature at which the maximum C_2Cl_4 concentration was reached) was detected and the maximum concentration was 50 ppm at T_{max} = 500 °C. Over the $0.89Au_{1.86}Pd/3DOM\ TiO_2$, $0.87Au_{0.95}Pd/3DOM\ TiO_2$, $0.91Au_{0.51}Pd/3DOM\ TiO_2$, $0.93Au/3DOM\ TiO_2$, and $0.89Pd/3DOM\ TiO_2$ samples, however, very low concentrations of C_2Cl_4 were detected and the maximum C_2Cl_4 concentrations were < 183 ppm.

The HCl selectivity (S_{HCl}) over all of the samples are also listed in Table 3. It is found that all of the samples showed a high HCl selectivity, particularly over the $0.91Au_{0.51}Pd/3DOM\ TiO_2$ sample. Since HCl is easier to be treated and less toxic than Cl_2, a high HCl selectivity would be favorable for the oxidation of TCE. Moreover, over each of the samples, selectivity to CO_x was higher than 99% (more than 98% CO_2 as well as a trace amount of CO). It should be noted that the estimated carbon and chlorine balance were 95–97 and 89–94%, respectively. In other words, small amounts of carbon and chlorine were retained on the surface of the samples.

2.6. Catalytic Stability and Effects of H_2O, CO_2, and HCl on Catalytic Activity

To test the stability of the catalyst, we implemented the on-stream TCE oxidation over $0.91Au_{0.51}Pd/3DOM\ TiO_2$ at 430 °C and SV = 20,000 mL/(g h). As shown in Figure 10, no significant loss in activity was observed after 30 h of on-stream reaction. This result demonstrates that $0.91Au_{0.51}Pd/3DOM\ TiO_2$ displayed good thermal stability in TCE oxidation. Due to the strong interaction between AuPd NPs and 3DOM TiO_2, the supported AuPd alloy sample exhibited excellent thermal stability [9], which would be useful in designing high-performance catalysts for practical removal of CVOCs.

Effects of water vapor, carbon dioxide, and hydrochloric acid on activity of the $0.91Au_{0.51}Pd/3DOM\ TiO_2$ sample at 410 °C and SV = 20,000 mL/(g h) were probed, and their results are shown in Figure 11A–C. Since water vapor is part of the feedstock and reaction products, it is necessary to explore the influence of water vapor on catalytic performance. It has been reported that activities of most of the catalysts were negatively influenced by water vapor introduction [19]. Therefore, it is highly desirable to generate water-resistant catalysts for industrial applications. Figure 11A shows the effect of water vapor (3.0 or 5.0 vol%) on performance of the $0.91Au_{0.51}Pd/3DOM\ TiO_2$ sample. In the presence of 3.0 vol% water vapor, TCE conversion decreased by ca. 5% after 5 h of on-stream reaction; a further rise in water vapor concentration to 5.0 vol% led to a drop in TCE conversion by ca. 13%. When water vapor was cut off, TCE conversions were basically recovered to the initial values in the absence of water vapor. This result manifests that partial deactivation induced by H_2O was reversible. The inhibition of water was due to the competitive adsorption of water and reactant molecules on

the active sites in the $0.91Au_{0.51}Pd/3DOM\ TiO_2$ sample, in which water adsorption is more likely to occur than TCE or oxygen. Figure 11B shows the effect of CO_2 addition on catalytic activity of $0.91Au_{0.51}Pd/3DOM\ TiO_2$ at 410 °C and 20,000 mL/(g h). Introduction of 5.0 and 10.0 vol% CO_2 to the reaction system led to ca. 4 and 7% loss in TCE conversion, respectively. The negative effect of CO_2 addition was due to the fact that partial active sites in $0.91Au_{0.51}Pd/3DOM\ TiO_2$ were covered by the adsorbed carbonate species formed during the on-stream reaction [19]. After the used sample was activated in an O_2 flow of 20 mL/min at 500 °C for 1 h, TCE conversion slightly increased. This result suggests that the formed carbonate species were not totally decomposed and part of the active sites occupied by the carbonate species were not recovered. Therefore, partial deactivation due to CO_2 addition was irreversible. Similar phenomena were also observed in our previous investigation [44]. When 100 ppm HCl was introduced to the reaction system, there was only a small loss in TCE conversion over the $0.91Au_{0.51}Pd/3DOM\ TiO_2$ sample below 410 °C (Figure 11C). The result reveals that this catalyst showed good resistance to HCl poisoning. Such a good hydrochloric acid resistance of $0.91Au_{0.51}Pd/3DOM\ TiO_2$ might be due to the fact that the highly dispersed AuPd NPs could effectively inhibited the chemisorption of HCl on the sample surface at higher temperatures.

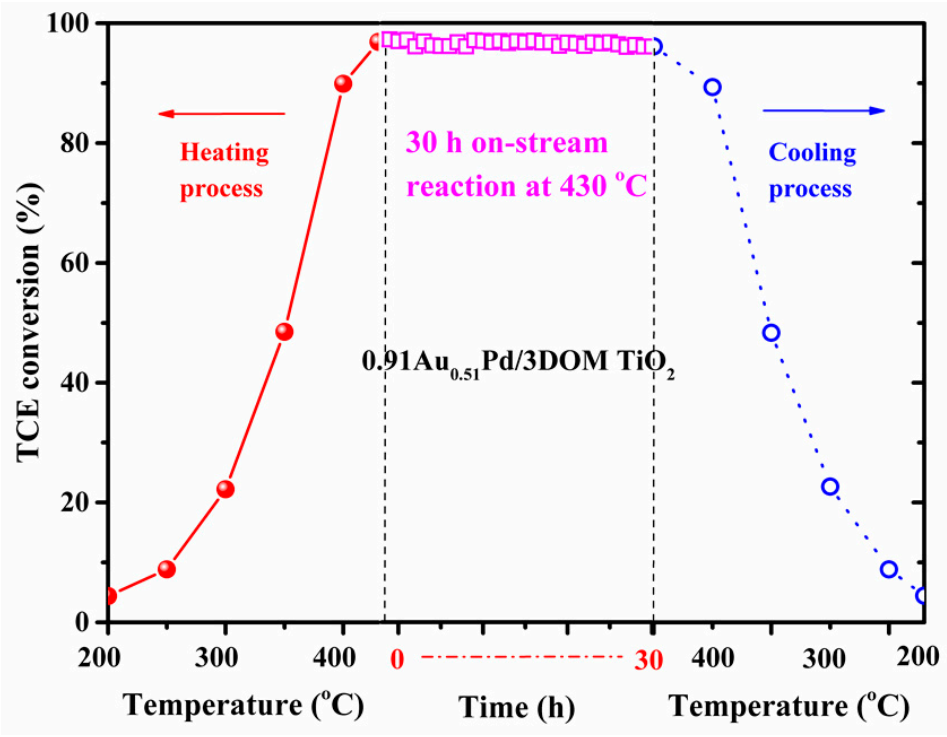

Figure 10. TCE conversion as a function of on-stream reaction time over $0.91Au_{0.51}Pd/3DOM\ TiO_2$ at 430 °C, and SV = 20,000 mL/(g h).

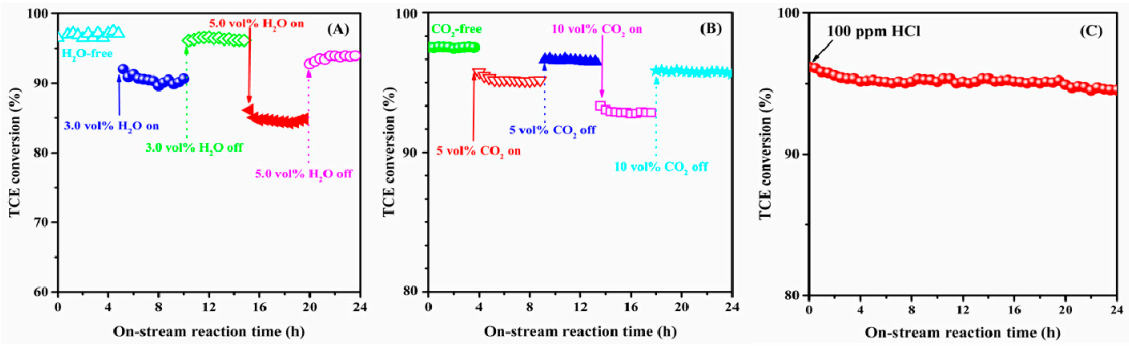

Figure 11. Effects of (**A**) water vapor, (**B**) carbon dioxide, and (**C**) hydrochloric acid on catalytic activity of $0.91Au_{0.51}Pd/3DOM\ TiO_2$ at 410 °C and SV = 20,000 mL/(g h).

2.7. Possible Reaction Pathway

In order to probe the mechanism of TCE oxidation, we recorded the in-situ DRIFT spectra of the $0.91Au_{0.51}Pd/3DOM\ TiO_2$ and 3DOM TiO_2 samples during the oxidation of TCE, as shown in Figure 12A,B. The in-situ DRIFT experiments were conducted over the $0.91Au_{0.51}Pd/3DOM\ TiO_2$ or 3DOM TiO_2 sample in a flow of the (O_2 + TCE) mixture gas (O_2/TCE molar ratio = 4) at different temperatures (100–450 °C). The negative absorption bands at 3740 and 3685 cm^{-1} were ascribed to the stretching vibration of hydroxyls groups [45–48]. A broad band at 3400 cm^{-1} due to the surface hydrogen-bonded hydroxyl groups appeared [49]. In the C-H stretching vibration region, several IR bands were obtained at 2974, 2941, and 2895 cm^{-1}, which belonged to the asymmetric stretching vibration ($\nu_{as}CH_3$), symmetric stretching vibration (ν_sCH_3), and symmetric stretching vibration (ν_sC-H) [47,48], respectively. The IR band at 2880 cm^{-1} was assigned to HCl [50], the one at 1690 cm^{-1} was ascribed to 2ν(C-Cl_2), whereas the one at 1620 cm^{-1} was due to $\delta(H_2O)$ of the adsorbed water [48]. The fundamental vibration bands of the C-H bonds were at 1380 cm^{-1} ($\delta(CH_2)$ or $\delta_s(CH_3)$) and 1356 cm^{-1} ($\delta_s(CH_3)$). A series of bands at 1581 and 1556 cm^{-1} (ν(C=C)), 1260 cm^{-1} (δ(CH-Cl)), 960 and 840 cm^{-1} (ν(C-Cl)), 790 cm^{-1} (ν(C=Cl)), and 735 cm^{-1} (ν(C-Cl_2)) [45–48,50] were due to the adsorption of TCE. In the low wavenumber region, there were also other weak IR bands between 1000 and 1400 cm^{-1}, assignable to the weak absorption due to the C-H and C-C vibrations [47,48]. The band at 1050 cm^{-1} was attributed to the oxygen–oxygen stretching vibration of the chemisorbed oxygen species [51]. It can be seen from Figure 12A that the IR spectrum changed distinctly with the rise in reaction temperature. The most noticeable alteration was the enhancement of HCl formation, as evidenced by recording of the characteristic band of HCl at 2880 cm^{-1} [50]. When the reaction temperature rose, intensity of the bands assignable to the molecular TCE absorption decreased, a result possibly due to the exothermic nature of adsorption and the enhanced kinetics of TCE at higher temperatures. The rise in temperature influenced the H-bonding affinity and caused the characteristic broad band between 3300–3500 cm^{-1} to first increase and then decrease in intensity (Figure 12A), but the characteristic band in Figure 12B increased continuously [49]. As the temperature went up, the molecular TCE bands became weaker and disappeared. The maximum difference in the DRIFT spectra of the two catalysts was the recorded band range of 750–1800 cm^{-1}. As reflected from the band at 1050 cm^{-1}, amount of the adsorption oxygen species of the supported AuPd catalysts was higher than that of the 3DOM TiO_2. These results suggest that TCE could be oxidized easier and a more amount of the adsorbed oxygen species was generated on the surface of $0.91Au_{0.51}Pd/3DOM\ TiO_2$. The results were the same as those of activity evaluation and O_2-TPD investigations. The recording of the band at 1480 cm^{-1} was indicative of presence of carboxylate species [45,51] on the surface of the two samples, and the intensity of this band was higher on the $0.91Au_{0.51}Pd/3DOM\ TiO_2$ sample (Figure 12A) than that on the 3DOM TiO_2 sample (Figure 12B), confirming again that AuPd was the active site of TCE adsorption, and TCE oxidation was more likely to occur at the interface between AuPd NPs and 3DOM TiO_2.

Based on the results reported by other researchers [45–52] and the results obtained in the present work, we propose the following TCE oxidation mechanisms over $0.91Au_{0.51}Pd/3DOM\ TiO_2$ and 3DOM TiO_2 (Equations (1)–(3)). The mechanism over $0.91Au_{0.51}Pd/3DOM\ TiO_2$ involved in an electron transfer from AuPd to 3DOM TiO_2. The gas-phase oxygen molecules were adsorbed on AuPd or 3DOM TiO_2 to form the surface active oxygen species, which attacked the intermediates of TCE to generate the oxygenate species, finally giving rise to the reaction products (CO_2, H_2O, HCl, and Cl_2 (Equation (1)). The bimetallic AuPd NPs in $0.91Au_{0.51}Pd/3DOM\ TiO_2$ could accelerate the reaction rate and enhance the deep oxidation of TCE, thus reducing formation of the byproducts. Moreover, the strength of the bond between the reactant or intermediate molecules and surface atoms could be modified by the electronic interaction between the surface atom and its neighbor. The gas-phase O_2 molecules were activated by picking up the electrons from 3DOM TiO_2 to form the adsorbed oxygen species, which could activate the C-Cl and C=C bonds and hence promoted the oxidation of TCE. The presence of AuPd alloy NPs was beneficial for generation of the adsorbed oxygen species,

and the enhanced oxidation ability of the sample could block the Cl addition of the C=C bond due to the fast C=C bond oxidation to CO_2. Therefore, the content of the chloric byproducts formed over $0.91Au_{0.51}Pd/3DOM\ TiO_2$ was much lower than that formed over 3DOM TiO_2. TiO_2 was not a good oxygen-donating agent due to its strong Ti–O bonds, which explained the low activity of TiO_2 for the oxidation of TCE. The C=C bond was too stable to be broken. On the contrary, the strong electronegativity of Cl weakened the C-Cl bond energy (396 kJ/mol), which was much lower than the C-H bond energy (485 kJ/mol). Hence, the first step in TCE oxidation was the dechlorination reaction. The chlorine in the reactant could be adsorbed on the surface as the Cl^- species or release from the sample surface as the HCl and/or Cl_2 products. In general, the stronger the redox ability, the higher the Deacon reaction rate. The Deacon reaction (Equation (2)) could promote the release of the Cl species on the catalyst surface, which depended on the redox property of a catalyst. Specifically, the C=C bond in TCE (as a Lewis base) was first activated and dissociated on the Lewis acid sites, followed by chlorination to form CCl_3CHCl_2 via the addition reaction; and then the HCl elimination reaction occurred with the H abstraction by a basic O^{2-} and the dissociation of the C-Cl bond. It should be noted that a small amount of perchloroethylene (PCE) as a byproduct was detected in the oxidation of TCE over $0.91Au_{0.51}Pd/3DOM\ TiO_2$ and 3DOM TiO_2 (Figure S4). Aranzabal et al. [52] pointed out that small amounts of PCE were generated during the destruction of TCE over the Pd/alumina catalysts. Feijen-Jeurissen et al. investigated the destruction mechanism of TCE over γ-Al_2O_3 and γ-Al_2O_3-supported chromium and palladium catalysts, and also observed formation of PCE [42]. These authors thought that the PCE byproduct was formed after the chlorination–dehydrochlorination processes (Equation (3)).

$$8CCl_2{=}CHCl + 17O_2 \rightarrow 16CO_2 + 2H_2O + 10Cl_2 + 4HCl \quad (1)$$

$$4HCl + O_2 \leftrightarrow 2Cl_2 + 2H_2O \quad (2)$$

$$CCl_2{=}\,CHCl \xrightarrow[M-Cl]{Cl_2\ or} CCl_3{-}CHCl_2 \xrightarrow{-HCl} CCl_2{=}\,CCl_2 \quad (3)$$

Since TCE contains an amount of chlorine atoms more than that of hydrogen atoms, Cl_2 can be formed in the absence of water. If the Deacon equilibrium is reached under the reaction conditions, the addition of water to the feed would reduce the amount of Cl_2 via the reverse Deacon reaction (Equation (2)). Therefore, very few molecular chlorine and chlorine on the catalyst surface could result in a reduced generation of PCE.

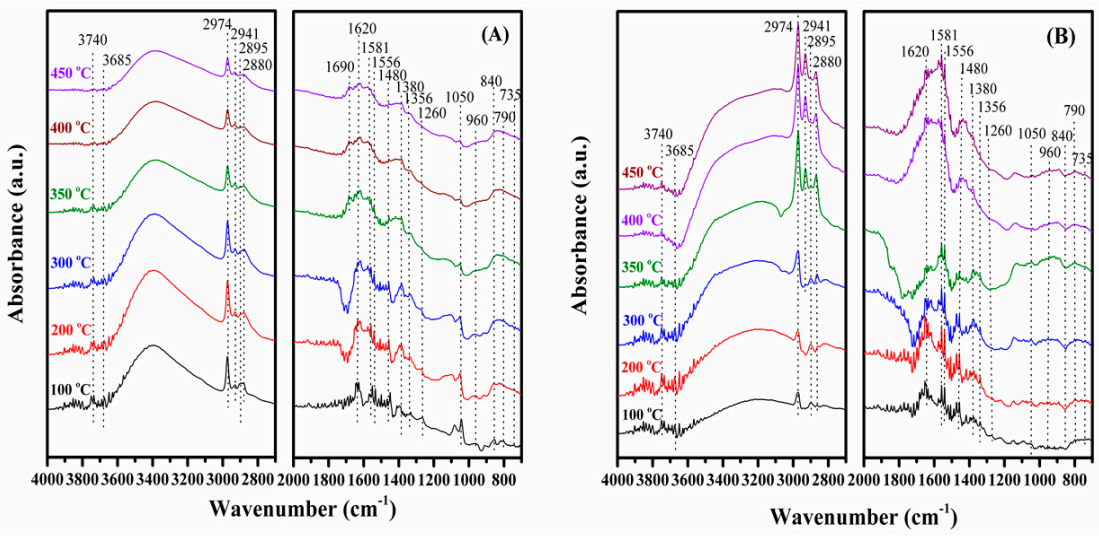

Figure 12. In-situ DRIFT spectra of (**A**) $0.91Au_{0.51}Pd/3DOM\ TiO_2$ and (**B**) 3DOM TiO_2 during TCE oxidation at different temperatures.

3. Materials and Methods

All of the reagents (A.R. in purity) in the present work were purchased from Beijing Chemical Reagent Company and used without any further purification. He, O_2, N_2 and Air used were 99.99% in purity.

3.1. Preparation of the Catalysts

Well-arrayed colloidal crystal PMMA microspheres with an average diameter of ca. 300 nm (Figure S1) were synthesized adopting the procedures described by Li et al. [53]. The 3DOM TiO_2 support was fabricated via the PMMA-templating route. The 3DOM TiO_2-supported AuPd alloy NPs (xAu$_y$Pd/3DOM TiO_2 (x is the total loading (wt%) of Au and Pd; y is the Pd/Au molar ratio)) samples were prepared using the gas bubble-aided polyvinyl alcohol (PVA)-protected reduction strategy with $NaBH_4$ as the reducing agent. The typical synthesis process is illustrated in Scheme S1. A certain amount of PVA was added to a $HAuCl_4$ and $PdCl_2$ mixed aqueous solution (0.01 mol/L) with the noble metal/PVA mass ratio of 1:1.2 in an ice bath under vigorous stirring. After the suspension was bubbled with a N_2 flow of 200 mL/min for 20 min, a $NaBH_4$ aqueous solution (0.1 mol/L) was rapidly injected to form a dark brown AuPd nanoparticle suspension with the noble metal/$NaBH_4$ molar ratio of 1:5. A desired amount of 3DOM TiO_2 was then added to the AuPd nanoparticle suspension with the theoretical Au$_y$Pd (y = 2, 1, 0.5) loading being ca. 1 wt%. The obtained suspension was treated ultrasonically (60 kHz) for 10 min. The gas bubble-aided stirring operation with a N_2 flow of 200 mL/min for 5 h was aimed to make the reaction homogenous. The wet precipitate was in turn filtered, washed with deionized water (2.0 L) and ethanol (1.0 L) to remove the adsorbed Cl^-, Na^+, and PVA, dried at 80 °C for 12 h, and calcined in an air flow of 100 mL/min at 500 °C for 2 h, thus generating the xAu$_y$Pd/3DOM TiO_2 samples. We made the inductively coupled plasma–atomic emission spectroscopic (ICP–AES) characterization of the samples, and found that the actual AuPd loadings (x) in xAu$_y$Pd/3DOM TiO_2 were 0.89, 0.87, and 0.91 wt%, the actual Au/Pd molar ratio (y) in the samples was 1.86, 0.95, and 0.51, and the actual Au and Pd loadings in xAu/3DOM TiO_2 and xPd/3DOM TiO_2 were 0.93 and 0.89 wt% (Table 1), respectively.

3.2. Catalytic Activity Evaluation

The catalytic activity of the samples was evaluated in a continuous-flow fixed-bed quartz microreactor with i.d. = 6 mm (Scheme S2). 50 mg of the sample (40–60 mesh) was mixed with 0.25 g of quartz sands (40–60 mesh) for minimization of the hot spots effect. Before measurement, the sample was treated in O_2 (20 mL/min) at 300 °C for 1 h. After being cooled to room temperature, the reactant gas mixture (750 ppm TCE + 20 vol% O_2 + N_2 (balance)) with a total flow rate of 16.7 mL/min was passed through the catalyst bed, giving a SV of ca. 20,000 mL/(g h). The pipe was heated to 100 °C using the heating band to minimize the possible adsorption of the TCE on the inner pipe surface. After the reaction was stabilized at a certain temperature for 30 min, the reactants and products were online analyzed by a gas chromatograph (GC-7890B, Agilent, Santa Clara, CA, USA) equipped with a flame ionization detector (FID) and a TCD, using the Agilent 19091J-413 HP-5 (30 m in length) and G3591-81141 and G3591-81142 (silica gel) and G3591-81022 (molsieve 5A) (2.44 m in length of each packing column). The TCD was used to analyze the CO_2 and CO concentrations, whereas the FID was used to analyze the concentrations of the organic compounds. TCE conversion is defined as $(c_{\text{inlet}} - c_{\text{outlet}})/c_{\text{inlet}} \times 100\%$, where the c_{inlet} and c_{outlet} are the inlet and outlet TCE concentrations in the feed stream. The possible reaction intermediates or products were detected online by the Agilent GC(5977A MSD)–MS(7890B) equipment. 3.0 and 5.0 vol% H_2O were introduced by passing the feed stream through a water saturator at 23 and 34 °C, respectively. In the case of CO_2 addition, 5.0 or 10 vol% CO_2 was introduced from a CO_2 gas cylinder. In the case of HCl introduction, 100 ppm HCl was fed from a gas cylinder (N_2 (balance)) to the reaction stream. The balance of carbon throughout the catalytic system was estimated to be 98.5 ± 1.5%.

Selectivities to HCl and Cl_2 were measured by bubbling the outlet gas mixture in a NaOH aqueous solution (12.5 mmol/L) for 0.5 h each time. The Cl_2 concentration in the bubbled solution was determined by chemical titration using ferrous ammonium sulfate with *N*,*N*-diethyl-*p*-phenylenediamine as indicator, and the Cl^- concentration was measured using an ion selective electrode [54]. The selectivities to HCl and Cl_2 were calculated according to the following formular: S_{HCl} = [HCl]/([HCl] + 2[Cl_2]) × 100% and S_{Cl2} = 2[Cl_2]/([HCl] + 2[Cl_2]) × 100%, where [Cl_2] and [HCl] are the outlet concentrations of Cl_2 and HCl, respectively.

3.3. Catalyst Characterization

Physicochemical properties of the samples were characterized by means of techniques, such as ICP–AES, X-ray diffraction (XRD), scanning electron microscopy (SEM), high-resolution transmission electron microscopy (HRTEM), high angle annular dark field and scanning transmission electron microscopy (HAADF–STEM), N_2 adsorption–desorption (BET), X-ray photoelectron spectroscopy (XPS) and curve-fitting method, hydrogen temperature-programmed reduction (H_2-TPR), oxygen temperature-programmed desorption (O_2-TPD), ammonia temperature-programmed desorption (NH_3-TPD), and in-situ diffuse reflectance infrared Fourier transform spectroscopy (DRIFTS). The detailed characterization procedures can be seen in the Supplementary material.

4. Conclusions

The 3DOM TiO_2 and xAu$_y$Pd/3DOM TiO_2 samples with a surface area of 49–53 m^2/g were prepared using the PMMA-templating and PVA-protected reduction methods, respectively. The supported bimetallic and 3DOM TiO_2 catalysts possessed a good-quality 3DOM architecture and an anatase crystal phase. The Au–Pd alloy NPs were 2.9–3.4 nm in average particle size and well dispersed on the skeleton surface of 3DOM TiO_2. An appropriate Au–Pd loading could increase the O_{ads} species concentration and enhance the low-temperature reducibility of xAu$_y$Pd/3DOM TiO_2. Among all of the samples, 0.91Au$_{0.51}$Pd/3DOM TiO_2 showed the highest catalytic activity ($T_{10\%}$ = 255 °C, $T_{50\%}$ = 354 °C, and $T_{90\%}$ = 400 °C at SV = 20,000 mL/(g h)) and good catalytic stability in TCE oxidation. The E_a values (51.7–66.2 kJ/mol) over xAu$_y$Pd/3DOM TiO_2 were lower than those (71.4–97.6 kJ/mol) over 3DOM TiO_2 and 0.93Au/3DOM TiO_2, with the 0.91Au$_{0.51}$Pd/3DOM TiO_2 sample possessing the lowest E_a (51.7 kJ/mol). The distinctive 3DOM structure, well dispersed noble metal NPs, and electron interaction within the bimetallic alloys were responsible for the good thermal stability of the xAu$_y$Pd/3DOM TiO_2 samples. Partial deactivation induced by water vapor was reversible, whereas CO_2 introduction resulted in irreversible deactivation of 0.91Au$_{0.51}$Pd/3DOM TiO_2; and addition of 100 ppm HCl to the reaction system exerted little impact on activity of 0.91Au$_{0.51}$Pd/3DOM TiO_2. In-situ DRIFTS investigations reveal that inclusion of Au in the Au–Pd bimetallic alloys altered the reaction pathway and reduced formation of PCE. It is concluded that the good catalytic performance of 0.91Au$_{0.51}$Pd/3DOM TiO_2 was associated with the high O_{ads} species concentration, good low-temperature reducibility, strong AuPd NPs–3DOM TiO_2 interaction, and more amount of strong acid sites.

Supplementary Materials: Supplementary data associated with this article can be found at http://www.mdpi.com/2073-4344/8/12/666/s1, Catalyst characterization procedures, Figure S1: SEM image of the well-aligned PMMA microspheres, Scheme S1: An illustration for the preparation of the 3DOM TiO_2 and its supported AuPd alloy samples, Scheme S2: An illustration of the quartz tubular microreactor for catalytic activity evaluation, Figure S2: Noble metal particle-size distributions of (A) 0.89Au$_{1.86}$Pd/3DOM TiO_2, (B) 0.87Au$_{0.95}$Pd/3DOM TiO_2, (C) 0.91Au$_{0.51}$Pd/3DOM TiO_2, (D) 0.89Pd/3DOM TiO_2, and (E) 0.93Au/3DOM TiO_2, Figure S3: (A) N_2 adsorption–desorption isotherms and (B) pore size distributions of (a) 3DOM TiO_2, (b) 0.89Au$_{1.86}$Pd/3DOM TiO_2, (c) 0.87Au$_{0.95}$Pd/3DOM TiO_2, (d) 0.91Au$_{0.51}$Pd/3DOM TiO_2, (e) 0.93Au/3DOM TiO_2, and (f) 0.89Pd/3DOM TiO_2, Figure S4. Concentrations of C_2Cl_4 formed over (a) 0.91Au$_{0.51}$Pd/3DOM TiO_2, (b) 0.89Pd/3DOM TiO_2, (c) 3DOM TiO_2, (d) 0.89Au$_{1.86}$Pd/3DOM TiO_2, (e) 0.87Au$_{0.95}$Pd/3DOM TiO_2, and (f) 0.93Au/3DOM TiO_2 at SV = 20,000 mL/(g h), Table S1: Data obtained by the curve-fitting of the XPS spectra of the samples, Table S2: TCE oxidation rates over the 0.91Au$_{0.51}$Pd/3DOM TiO_2 and various catalysts reported in the literature.

Author Contributions: Conceptualization, H.D.; Methodology, X.Z. and Y.L.; Software, X.Z. and Z.H.; Investigation, K.Z. and Y.L.; Resources, H.D.; Data Curation, X.Z. and J.Y.; Writing—Original Draft Preparation, X.Z.; Writing—Review & Editing, X.Z.; Visualization, J.D.; Supervision, H.D.; Project Administration, H.D.; Funding Acquisition, H.D.

Funding: This work was supported by the National Natural Science Foundation of China (21677004 and 21876006), Beijing Nova Program (Z141109001814106), and Natural Science Foundation of Beijing Municipal Commission of Education (KM201410005008).

Conflicts of Interest: The authors declare no conflict of interest.

References

1. Pitkaaho, S.; Nevanpera, T.; Matejova, L.; Ojala, S.; Keiski, R.L. Oxidation of perchloroethylene over Pt, Pd, Rh, and V_2O_5 catalysis supported on Al_2O_3, Al_2O_3-TiO_2, and Al_2O_3-CeO_2. *Appl. Catal. B* **2013**, *138–139*, 33–42. [CrossRef]
2. Miranda, B.; Diaz, E.; Ordonez, S.; Diez, F.V. Catalytic combustion of trichloroethene over Ru/AlO: Reaction mechanism and kinetic study. *Catal. Commun.* **2006**, *7*, 945–949. [CrossRef]
3. Zhou, G.L.; Lan, H.; Song, R.Y.; Xie, H.M.; Du, Q.X. Effects of preparation method on CeCu oxide catalyst performance. *RSC Adv.* **2014**, *4*, 50840–50850. [CrossRef]
4. Maupin, I.; Pinard, L.; Mijoin, J.; Magnoux, P. Bifunctional mechanism of dichloromethane oxidation over Pt/Al_2O_3: CH_2Cl_2 disproportionation over alumina and oxidation over platinum. *J. Catal.* **2012**, *291*, 104–109. [CrossRef]
5. Rivas, B.; Lopez-Fonseca, R.; Jimenez-Gonzalez, C.; Gutierrez-Ortiz, J.I. Highly active behaviour of nanocrystalline Co_3O_4 from oxalate nanorods in the oxidation of chlorinated short chain alkanes. *Chem. Eng. J.* **2012**, *184*, 184–192. [CrossRef]
6. Pitkäaho, S.; Matejova, L.; Ojala, S.; Gaalova, J.; Keiski, R.L. Catalytic abatement of trichloroethylene over Mo and/or W-based bronzes. *Appl. Catal. B* **2012**, *111–114*, 150–159. [CrossRef]
7. Hutchings, G.J. Activated–carbon–supported gold–cesium(I) as highly effective catalysts for hydrochlorination of acetylene to vinyl chloride. *J. Catal.* **1985**, *96*, 292–295. [CrossRef]
8. Liu, Y.X.; Dai, H.X.; Deng, J.G.; Li, X.W.; Wang, Y.; Arandiyan, H.; Guo, G.S. Au/3DOM $La_{0.6}Sr_{0.4}MnO_3$: Highly active nanocatalysts for the oxidation of carbon monoxide and toluene. *J. Catal.* **2013**, *305*, 146–153. [CrossRef]
9. Liu, Y.X.; Dai, H.X.; Deng, J.G.; Xie, S.H.; Yang, H.G.; Tan, W.; Han, W.; Jiang, Y.; Guo, G.S. Mesoporous Co_3O_4-supported gold nanocatalysts: Highly active for the oxidation of carbon monoxide, benzene, toluene, and *o*-xylene. *J. Catal.* **2014**, *309*, 408–418. [CrossRef]
10. Saiman, M.I.B.; Brett, G.L.; Tiruvalam, R.; Forde, M.M.; Sharples, K.; Thetford, A.; Jenkins, R.L.; Dimitratos, N.; Lopez-Sanchez, J.A.; Murphy, D.M.; et al. Involvement of surface-bound radicals in the oxidation of toluene using supported Au−Pd nanoparticles. *Angew. Chem.* **2012**, *51*, 5981–5985. [CrossRef] [PubMed]
11. Enache, D.I.; Edwards, J.K.; Landon, P.; Solsona-Espriu, B.; Carley, A.F.; Herzing, A.A.; Watanabe, M.; Kiely, C.J.; Knight, D.W.; Hutchings, G.J. Bimetallic palladium–gold nanoparticl es synthesized in ionic liquid microemulsion. *Science* **2006**, *311*, 362–365. [CrossRef] [PubMed]
12. Chen, J.; Arandiyan, H.; Gao, X.; Li, J. Recent advances in catalysts for methane combustion. *Catal. Surv.* **2015**, *19*, 140–171. [CrossRef]
13. Zhang, Q.Y.; Gao, T.T.; Andino, J.M.; Li, Y. Copper and iodine co-modified TiO_2 nanoparticles for improved activity of CO_2 photoreduction with water vapor. *Appl. Catal. B* **2012**, *123–124*, 257–264. [CrossRef]
14. Zheng, Y.; Li, K.; Wang, H.; Wang, Y.; Tian, D.; Wei, Y.; Zhu, X.; Zeng, C.; Luo, Y. Structure dependence and reaction mechanism of CO oxidation: A model study on macroporous CeO_2 and CeO_2–ZrO_2 catalysts. *J. Catal.* **2016**, *344*, 365–377. [CrossRef]
15. Xie, S.H.; Deng, J.G.; Zang, S.M.; Yang, H.G.; Guo, G.S.; Arandiyan, H.; Dai, H.X. Au–Pd/3DOM Co_3O_4: Highly active and stable nanocatalysts for toluene oxidation. *J. Catal.* **2015**, *322*, 38–48. [CrossRef]
16. Xie, S.H.; Deng, J.G.; Liu, Y.X.; Zhang, Z.H.; Yang, H.G.; Jiang, Y.; Arandiyan, H.; Dai, H.X.; Au, C.T. Excellent catalytic performance, thermal stability, and water resistance of 3DOM Mn_2O_3-supported Au–Pd alloy nanoparticles for the complete oxidation of toluene. *Appl. Catal. A* **2015**, *507*, 82–90. [CrossRef]

17. Wang, Y.; Arandiyan, H.; Scott, J.; Akia, M.; Dai, H.X.; Deng, J.G.; Amal, R. High performance Au−Pd supported on 3D hybrid strontium-substituted lanthanum manganite perovskite catalyst for methane combustion. *ACS Catal.* **2016**, *6*, 6935–6947. [CrossRef]
18. Jiao, J.Q.; Wei, Y.C.; Zhao, Z.; Zhong, W.J.; Liu, J.; Li, J.M.; Jiang, G.Y. Synthesis of 3D ordered macroporous TiO_2-supported Au nanoparticle photocatalysts and their photocatalytic performances for the reduction of CO_2 to methane. *Catal. Today* **2015**, *258*, 319–326. [CrossRef]
19. Arandiyan, H.; Dai, H.X.; Ji, K.M.; Sun, H.Y.; Li, J.H. Pt nanoparticles embedded in colloidal crystal template derived 3D ordered macroporous $Ce_{0.6}Zr_{0.3}Y_{0.1}O_2$: Highly efficient catalysts for methane combustion. *ACS Catal.* **2015**, *5*, 1781–1793. [CrossRef]
20. Liu, Y.; Liu, B.C.; Wang, Q.; Li, C.Y.; Hu, W.T.; Liu, Y.X.; Jing, P.; Zhao, W.Z.; Zhang, J. Three-dimensionally ordered macroporous Au/CeO_2–Co_3O_4 catalysts with mesoporous walls for enhanced CO preferential oxidation in H_2-rich gases. *J. Catal.* **2012**, *296*, 65–76. [CrossRef]
21. Wei, Y.C.; Liu, J.; Zhao, Z.; Chen, Y.S.; Xu, C.M.; Duan, A.J.; Jiang, G.Y.; He, H. Highly active catalysts of gold nanoparticles supported on three-dimensionally ordered macroporous $LaFeO_3$ for soot oxidation. *Angew. Chem. Int. Ed.* **2011**, *50*, 2326–2329. [CrossRef] [PubMed]
22. Priolkar, K.R.; Bera, P.; Sarode, P.R.; Hegde, M.S.; Emura, S.; Kumashiro, R.; Lalla, N.P. In situ preparation and investigation of Pd/CeO_2 catalysts for the low-temperature oxidation of CO. *Chem. Mater.* **2002**, *14*, 2120–2128. [CrossRef]
23. Kesavan, L.; Tiruvalam, R.; Rahim, M.H.A.; Enache, D.I.; Jenkins, R.L.; Dimitratos, N.; Lopez-Sanchez, J.A.; Taylor, S.H.; Knight, D.W.; Kiely, C.J.; et al. Solvent free oxidation of primary carbon-hydrogen bonds in toluene using Au−Pd alloy nanoparticles. *Science* **2011**, *331*, 195–199. [CrossRef] [PubMed]
24. Zhang, L.; Li, L.; Cao, Y.; Yao, X.; Ge, C.; Gao, F.; Deng, Y.; Tang, C.; Dong, L. Getting insight into the influence of SO_2 on TiO_2/CeO_2 for the selective catalytic reduction of NO by NH_3. *Appl. Catal. B* **2015**, *165*, 589–598. [CrossRef]
25. Arandiyan, H.; Dai, H.X.; Deng, J.G.; Liu, Y.X.; Bai, B.Y.; Wang, Y.; Li, X.W.; Xie, S.H.; Li, J.H. Three-dimensionally ordered macroporous $La_{0.6}Sr_{0.4}MnO_3$ with high surface areas: Active catalysts for the combustion of methane. *J. Catal.* **2013**, *307*, 327–339. [CrossRef]
26. Batzill, M.; Diebold, U. Electronic properties of post-transition metal oxide semiconductor surfaces. *Prog. Surf. Sci.* **2005**, *79*, 47–154. [CrossRef]
27. Xie, S.H.; Liu, Y.X.; Deng, J.G.; Zhao, X.T.; Yang, J.; Zhang, K.F.; Han, Z.; Arandiyan, H.; Dai, H.X. Effect of transition metal doping on the catalytic performance of Au–Pd/3DOM Mn_2O_3 for the oxidation of methane and *o*-xylene. *Appl. Catal. B* **2017**, *206*, 221–232. [CrossRef]
28. Lucas, A.D.; Cañizares, P.; Durán, A. Improving deactivation behaviour of HZSM-5 catalysts. *Appl. Catal. A* **2001**, *206*, 87–93. [CrossRef]
29. Steltenpohl, P.; Aranzabal, A.; López-Fonseca, R.; Gutiérrez-Ortiz, J.I.; González-Velasco, J.R. Performance of zeolites and product selectivity in the gas-phase oxidation of 1,2-dichloroethane. *Catal. Today* **2000**, *62*, 367–377.
30. López-Fonseca, R.; Cibrián, S.; Gutiérrez-Ortiz, J.I.; Gutiérrez-Ortiz, M.A.; González-Velasco, J.R. Oxidative destruction of dichloromethane over protonic zeolites. *AIChE J.* **2010**, *49*, 496–504. [CrossRef]
31. Yang, P.; Zuo, S.F.; Shi, Z.N.; Tao, F.; Zhou, R.X. Accelerating effect of ZrO_2 doping on catalytic performance and thermal stability of CeO_2–CrO_x mixed oxide for 1,2-dichloroethane elimination. *Appl. Catal. B* **2016**, *191*, 53–61. [CrossRef]
32. Miranda, B.; Díaz, E.; Ordóñ ez, S.; Vega, A.; Díez, F.V. Performance of alumina-supported noble metal catalysts for the combustion of trichloroethene at dry and wet conditions. *Appl. Catal. B* **2006**, *64*, 262–271. [CrossRef]
33. Maghsoodi, S.; TowFigurehi, J.; Khodadadi, A.; Mortazavi, Y. Highly active Fe_2O_3-doped TiO_2 photocatalyst for degradation of trichloroethylene in air under UV and visible light irradiation: Experimental and computational studies. *Chem. Eng. J.* **2013**, *215*, 827–837. [CrossRef]
34. Weng, X.L.; Weng, P.F.; Long, Y.; Meng, Q.J.; Wu, Z.B. Catalytic oxidation of chlorobenzene over $Mn_xCe_{1-x}O_2$/HZSM-5 catalysts: A study with practical implications. *Environ. Sci. Technol.* **2017**, *51*, 8057–8066. [CrossRef] [PubMed]
35. Ordóñez, S.; Vega, A.; Miranda, B.; Díaz, E.; Díez, F.V. Oxidation of trichloroethene over metal oxide catalysts: Kinetic studies and correlation with adsorption properties. *Chemosphere* **2007**, *66*, 1706–1715.

36. Li, H.F.; Lu, G.Z.; Dai, Q.G.; Wang, Y.Q.; Guo, Y.; Guo, Y.L. Efficient low-temperature catalytic combustion of trichloroethylene over flower-like mesoporous Mn-doped CeO_2 microspheres. *Appl. Catal. B* **2011**, *102*, 475–483. [CrossRef]
37. Wang, J.; Liu, X.L.; Zeng, J.L.; Zhu, T.Y. Catalytic oxidation of trichloroethylene over TiO_2 supported ruthenium catalysts. *Catal. Commun.* **2016**, *76*, 13–18. [CrossRef]
38. Rivas, B.; Sampedro, C.; García-Real, M.; López-Fonseca, R.; Gutiérrez-Ortiz, J.I. Promoted activity of sulphated Ce/Zr mixed oxides for chlorinated VOC oxidative abatement. *Appl. Catal. B* **2013**, *129*, 225–235. [CrossRef]
39. Yang, P.; Shi, Z.N.; Yang, S.S.; Zhou, R.X. High catalytic performances of CeO_2–CrO_x catalysts for chlorinated VOCs elimination. *Chem. Eng. Sci.* **2015**, *126*, 361–369. [CrossRef]
40. Wu, M.; Dai, Q.G.; Wang, X.Y. Alumina hollow microspheres supported gold catalysts for low-temperature CO oxidation: Effect of the pretreatment atmospheres on the catalytic activity and stability. *Catal. Commun.* **2012**, *18*, 72–75. [CrossRef]
41. Gutiérrez-Ortiz, J.I.; López-Fonseca, R.; Aurrekoetxea, U.; González-Velasco, J.R. Low-temperature deep oxidation of dichloromethane and trichloroethylene by H-ZSM-5-supported manganese oxide catalysts. *J. Catal.* **2003**, *218*, 148–154. [CrossRef]
42. Feijen-Jeurissen, M.M.R.; Jornaa, J.J.; Nieuwenhuysa, B.E.; Sinquinb, G. Mechanism of catalytic destruction of 1,2-dichloroethane and trichloroethylene over γ-Al_2O_3 and γ-Al_2O_3 supported chromium and palladium catalysts. *Catal. Today* **1999**, *54*, 65–79. [CrossRef]
43. Blanch-Raga, N.; Palomares, A.E.; Martínez-Triguero, J.; Puche, M.; Fetter, G.; Bosch, P. The oxidation of trichloroethylene over different mixed oxides derived from hydrotalcites. *Appl. Catal. B* **2014**, *160–161*, 129–134. [CrossRef]
44. Burch, R.; Urbano, F.J.; Loader, P.K. Methane combustion over palladium catalysts: The effect of carbon dioxide and water on activity. *Appl. Catal. A* **1995**, *123*, 173–184. [CrossRef]
45. Datka, J.; Sarbak, Z.; Eischens, R.P. Infrared study of coke on alumina and zeolite. *J. Catal.* **1994**, *145*, 544–550. [CrossRef]
46. Kagel, R.O. Infrared investigation of the adsorption and surface reactions of the C1 through C4 normal alcohols on γ-alumina. *J. Phys. Chem.* **1967**, *71*, 844–850. [CrossRef]
47. Eisenbach, D.; Gallei, E. Infrared spectroscopic investigations relating to coke formation on zeolites: I. Adsorption of hexene-1 and n-hexane on zeolites of type Y. *J. Catal.* **1979**, *56*, 377–389. [CrossRef]
48. Trombetta, M.; Busca, G.; Rossini, S.A.; Piccoli, V.; Cornaro, U. FT-IR studies on light olefin skeletal isomerization catalysis.1. The interaction of C4 olefins and alcohols with pure gamma-alumina. *J. Catal.* **1997**, *168*, 334–348. [CrossRef]
49. Phillips, L.A.; Raupp, G.B. Infrared spectroscopic investigation of gas–solid heterogeneous photocatalytic oxidation of trichloroethylene. *J. Mol. Catal.* **1992**, *77*, 297–311. [CrossRef]
50. Halasz, J.; Imre, B.; Hannus, I. IR spectroscopic investigation of hydrodechlorination on Pt-containing zeolites. *Appl. Catal. A* **2004**, *27*, 47–53. [CrossRef]
51. Schmal, M.; Mariana Souza, M.V.M.; Alegre, V.V.; Monica Silva, A.P.D.; Cesar, D.V.; Perez, C.A.C. Methane oxidation–effect of support, precursor and pretreatment conditions—In situ reaction XPS and DRIFT. *Catal. Today* **2006**, *118*, 392–401. [CrossRef]
52. Aranzabal, A.; Ayastuy-Arizti, J.L.; González-Marcos, J.A.; González-Velasco, J.R. The reaction pathway and kinetic mechanism of the catalytic oxidation of gaseous lean TCE on Pd/alumina catalysts. *J. Catal.* **2003**, *214*, 130–135. [CrossRef]
53. Li, H.N.; Zhang, L.; Dai, H.X.; He, H. Facile synthesis and unique physicochemical properties of three-dimensionally ordered macroporous magnesium oxide, gamma-alumina, and ceria-zirconia solid solutions with crystalline mesoporous walls. *Inorg. Chem.* **2009**, *48*, 4421–4434. [CrossRef] [PubMed]
54. Yang, P.; Xue, X.M.; Meng, Z.H.; Zhou, R.X. Enhanced catalytic activity and stability of Ce doping on Cr supported HZSM-5 catalysts for deep oxidation of chlorinated volatile organic compounds. *Chem. Eng. J.* **2013**, *234*, 203–210. [CrossRef]